JTTEE5 9:377-388

Microstructural Characterization of Superaustenitic Stainless Steel Surface Alloys Formed Using Laser Treatment

K. Sridhar, M.B. Deshmukh, A.S. Khanna, and A. Gasser

(Submitted 31 March 1999; in revised form 26 December 1999)

Conventional stainless steels (SS's) such as AISI type 304 SS are used in many industrial applications due to their excellent weldability and good mechanical properties. However, in contacts with chlorides, they suffer from localized corrosion. AISI type 304 SS was alloyed at the surface with chromium, nickel, and molybdenum using a CO_2 laser carried under varying laser processing parameters. The objective is to create a surface alloy with composition and microstructure, suitable for marine environments. The surface alloys were characterized using optical microscopy and scanning electron microscopy (SEM) and revealed the presence of the austenitic phase. Analysis by SEM-energy dispersive analysis (EDAX) revealed good compositional homogeneity with molybdenum contents in the range of 3 to 15 wt.%. The dendrite arm spacing (DAS) measured at the surface and bottom of the surface alloy using an image analyzer was found to be in good correlation with calculated cooling rates.

Keywords cooling rate, dendrite arm spacing, laser surface alloying, post-processing, superaustenitic steel

1. Introduction

Conventional grades of austenitic stainless steel (SS), *viz.*, type AISI 304, are widely used because of their good mechanical properties and excellent weldability. However, their susceptibility to pitting and crevice corrosion in chloride environments is an important limitation.[1] Molybdenum is reported to enhance the resistance against localized corrosion for these steels. Even the improved grades, *viz.*, type AISI 316 SS, containing molybdenum in the range of 2 to 3 wt.% have only limited service life in offshore applications.

Highly alloyed austenitic stainless steels, containing molybdenum in the range of 6 to 7 wt.%, with increased Ni and Cr content and small additions of nitrogen have been reported to have excellent localized corrosion resistance in chloride environments, such as seawater.[2] These highly alloyed SS's containing high molybdenum contents are, however, susceptible to the formation of undesirable secondary phases. These phases are not beneficial for mechanical properties and also affect the corrosion behavior.[3] Also, the interface between these phases and the matrix may be depleted in molybdenum and chromium, therefore, rendering them susceptible to pitting corrosion.[4]

Corrosion is a surface phenomenon, and, therefore, modification of chemical composition and microstructure at the surface of stainless steels would be a desirable technique to form a high performance surface alloy. In order to overcome the problems related to fabrication, welding, and corrosion properties of conventionally, highly alloyed austenitic stainless steels, surface alloying is generally adopted. Conventional surface alloying methods such as ion implantation suffer from drawbacks such as porosity and poor adhesion to the substrate.

Laser surface alloying (LSA) is a technique characterized by rapid heating and cooling rates. The structure of coatings is often pore-free and exhibits good metallurgical bonding to the substrate. Hence, LSA is an appropriate method to create high performance surface alloys. These alloys have a fine cellular microstructure with no segregation, even with high amounts of desired elements, alloyed onto the surface. This microstructure is obtained due to high cooling rates, and, in addition, high concentration of the desired alloying elements is achieved at the surface.[5] The surface alloy obtained is metallurgically bonded to the substrate, and it is possible to modify the microstructure and the concentration of the elements by varying the process parameters. Because of the rapid solidification and high cooling rates, formation of undesirable secondary phases (which contain high chromium and molybdenum contents) such as sigma and chi is highly minimized or eliminated.[6] Laser surface alloying could lead to reduced consumption of strategic materials such as Mo and Ni, since an alloyed depth of 250 to 300 μm is sufficient for most applications.

The intent of the present work is to form a molybdenum-rich surface alloy to obtain maximum resistance to localized corrosion. For this purpose, commercially available Ni-Cr and Mo powders and their composition were exploited, and a properly chosen composition and thickness of these elements in powder form were preplaced on 304 SS by plasma spraying. Since the austenitic phase is favored for improved corrosion resistance in marine environments, the amount of austenitic stabilizing nickel was increased in conjunction with ferrite stabilizing molybdenum. This coating is expected to form austenitic with high molybdenum contents on subsequent alloying with lasers.

The main objective was to form a superaustenitic surface alloy AISI type 304 SS substrate by LSA for improved corrosion resis-

K. Sridhar and **M.B. Deshmukh,** Naval Materials Research Laboratory, Naval Dockyard, Bombay - 400 023, India; **A.S. Khanna,** Corrosion Science and Engineering, Indian Institute of Technology, Bombay - 400 076, India; and **A. Gasser,** Fraunhofer Institut for LaserTechnik, Steinbachtrasse, Aachen, Germany. Contact e-mail: sudi@bom4.vsnl.net.in.

tance in aqueous chloride environments. The major constituent of surface alloy is molybdenum, which enhances the pitting and crevice corrosion resistance of stainless steels. Formation of such surface alloys using various laser parameters such as laser power, scan speed (interaction time), and spot size was carried out to establish the effect of these parameters on the properties of the laser-alloyed zone. The optimum parameter could thus be obtained by carrying out systematic microstructural studies: composition analysis and corrosion behavior of the laser-alloyed zones.

2. Experimental Methods

2.1 Materials and Surface Alloying

The samples of size $10 \times 10 \times 0.4$ cm thickness were cut from SS 304 sheet. The composition of 304 SS as determined by wet chemical analysis is shown in Table 1. The samples were polished with 320 and 600 grit silicon carbide paper and rinsed with acetone. With the commercially available Ni-Cr and Mo powders, the thicknesses of the coating of Ni-Cr and Mo were chosen such that the surface alloy formed (after laser processing) contains an optimum concentration of major alloying elements; Ni, Cr, and Mo.

Samples of 304 SS were plasma coated using Metco (US) 60 kW equipment at a stand-off distance of 150 mm. Powders of Ni-Cr (80-20 wt.%) and Mo (100 wt.%) were sprayed to a thickness of 80 and 40 μm, respectively. The samples were then fixed to a CNC controlled X–Y table and laser treated with a 5 kW ROFIN-SINAR (Germany) continuous wave CO_2 laser (10.6 μm) by varying process parameters such as power, scan speed, and spot size (Table 2).

2.2 Microstructural Analysis

The laser-surface-alloyed samples were cut transversely and mounted in resin and polished to a 1 μm diamond finish. These were then etched in methonalic aqua regia (10 mL HCl, 5 mL HNO_3, and 8 mL CH_3OH) for optical metallography. Also, the samples were etched for 30 s in a modified boiling Murakami's reagent (30 g KOH, 30 g K_3FeCN_6, and 100 mL H_20) in order to delineate any second-phase constituents such as sigma and chi. Scanning electron microscopic observation of the samples etched with methanolic aquaregia was carried out to determine the microstructure at higher magnification at different locations of the alloyed zone.

Characterization by x-ray diffraction (XRD) using Cu K_α radiation of the laser-processed samples was carried out using a Rigaku x-ray diffractometer (Japan). The samples were polished (1 μm diamond finish) to remove the surface oxide.

The dimensional parameters of the laser-alloyed zone such as width and depth of the pool were measured using a LECO image analyzer (LECO Corporation, St. Joseph, MI). Also the primary dendritic arm spacing, both at the top and bottom of the laser-alloyed zones, processed under varying laser parameters, was measured to ascertain the cooling rate.

Table 1 Composition of the substrate (304 SS) in wt.%

Fe	Cr	Ni	Mn	Si	Mo	P	C	S	Cr_{eq}	Ni_{eq}
Bal	19.37	9.14	1.60	0.49	0.02	0.02	0.02	0.01	20.13	10.54

The microhardness (VHN) measurements were taken on the etched transverse cross section of the laser-alloyed zone using a load of 200 g, which was applied for a duration of 15 s. Five measurements in each laser-alloyed zone were taken at regular intervals, and the average of these five values was reported as the hardness of the laser-alloyed zone.

The chemical composition of the laser-alloyed samples, mounted in a transverse direction, was determined using a Philips scanning electron microscope (Philips Electronic Instruments, Mahwah, NJ) with energy dispersive analysis (EDAX) at the center of the pool. The average chemical composition was determined from three fields taken from top to bottom of the alloyed zone, at its center, each of area 200×200 μm (for smaller alloyed depths) or 300×300 μm (for higher alloyed depths). Also, the chemical compositions of the laser surface alloys (mounted in the transverse direction), processed with varying scan speeds at a power level of 3 kW (LSA-1 to LSA-4) with respect to alloying elements Cr, Ni, Mo, and Fe, were determined at successive intervals of 50 μm using EDAX in a scanning electron microscope.

3. Results and Discussion

3.1 Microstructural Behavior

The microstructure of the laser-alloyed zone of all the experimental samples exhibited a fine cellular dendritic structure with

Table 2 Designation of laser of alloyed samples

Table 2.1 Variation in scan speed

Sample number	Scan speed (mm/min)	Melt depth (μm)	Melt width (μm)
LSA-1	500	405	6264
LSA-2	750	383	6392
LSA-3	1000	361	5969
LSA-4	1250	432	6096

Power (P) = 3 kW, area ($B \times L$) = 0.5×6 mm, and power density (P_d) = 10^5 W/cm^2

Table 2.2 Variation in power

Sample number	Laser power (kW)	Melt depth (μm)	Melt width (μm)
LSA-5	1	364	5987
LSA-6	2	431	5984
LSA-2	3	383	6392
LSA-7	4	425	6260

Scan speed (S) = 750 mm/min, area ($B \times L$) = 0.5×6 mm, and interaction time (IT) = B/S = 0.0396 s

Table 2.3 Variation in spot size

Sample number	Defocused beam area (mm^2)	Melt depth (μm)	Melt width (μm)
2	0.5×6	383	6392
9	0.75×6	649	6224
8	1.0×6	683	6270

Power (P) = 3 kW, scan speed (S) = 750 mm/min, and heat input (HI) = P/S = 240 J/mm

varying cell sizes, depending on the processing parameters employed in forming the surface alloys. The columnar growth was found at the interface of the base metal/laser-alloyed zone and at the laser-alloyed zone/ambient environment and arose due to the higher cooling rates experienced by the sample at these locations. At the center, a fine cellular dendritic microstructure of austenite was observed where the cooling rate is lower than that at the interface. The microstructures of the austenitic phase at the center of the laser-alloyed region for samples of various scan speeds (500, 750, 1000, and 1250 mm/min) at a constant power of 3 kW are shown in Fig. 1(a) to (d). The microstructure at the center of the laser-alloyed zones of samples revealed fine cells, which decreased in size from 5 to 2.5 μm with increasing scan speed due to decreasing interaction time and reduced heat input. The finer the cells, the better is homogeneity.

The optical micrograph of the entire defect free-alloyed zone at a scan speed of 1250 mm/min is shown in Fig 2(a). Figure 2(b) shows the same alloy at higher magnification and indicates the finer cells and columnar growth at the interface between the matrix and laser-alloyed zone. Previous studies[7] indicate that alloying of pure molybdenum using a pulsed Nd:YAG laser results in a duplex microstructure associated with severe cracking /porosity in the alloyed zone. The defects could be eliminated only by preheating of the sample. In the present study, increased nickel and molybdenum not only eliminated the cracks, but also favored the formation of the desired superaustenitic microstructure.

The microstructure near the interface region of the laser-alloyed zone and the base metal revealed the same grain size as that of the base metal for all samples (LSA-1 to LSA-9) indicating that there is no grain growth or heat-affected zone. This was also confirmed by the microhardness measurements at the interface and interior of the base metal. However, the partially melted zone existed at both the left and right ends of the sample. The width of this region was found to decrease with increasing scan speed of the laser beam. This could be attributed to the decreasing heat input, on increasing the scan speed. The variation of microhardness with varying molybdenum content and Mo/Ni ratio is depicted in Fig. 3. The microhardness of the laser-alloyed zone increases with increasing molybdenum content (Table 3). This is attributed to substitutional solid solution strengthening, which is the main strengthening mechanism, since no secondary phase of molybdenum compounds is found in the laser-alloyed region.[8] Substructure strengthening should also significantly con-

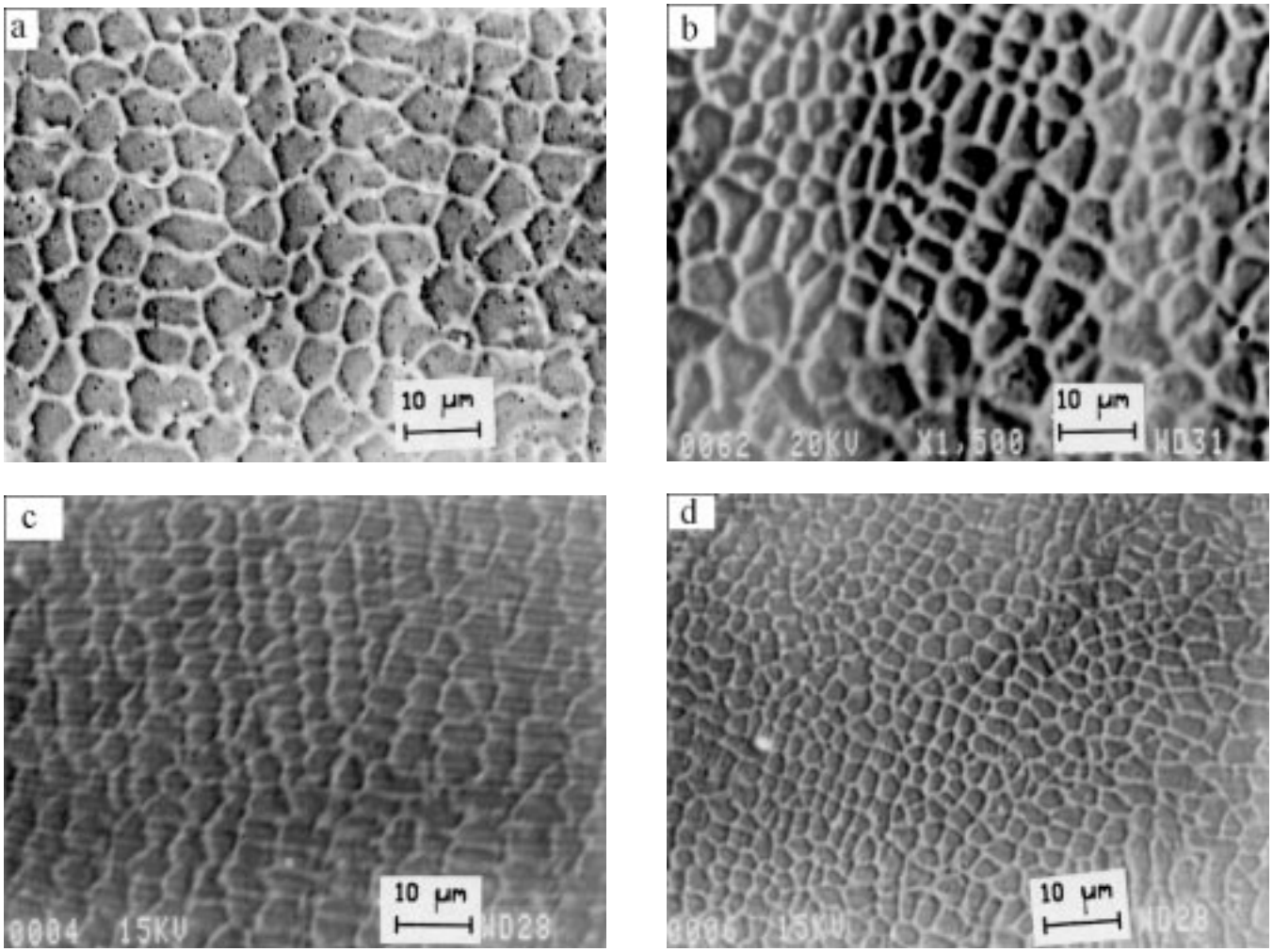

Fig. 1 SEM micrograph showing varying cell sizes at the center of the laser-alloyed samples: (**a**) LSA-1, (**b**) LSA-2, (**c**) LSA-3, and (**d**) LSA-4

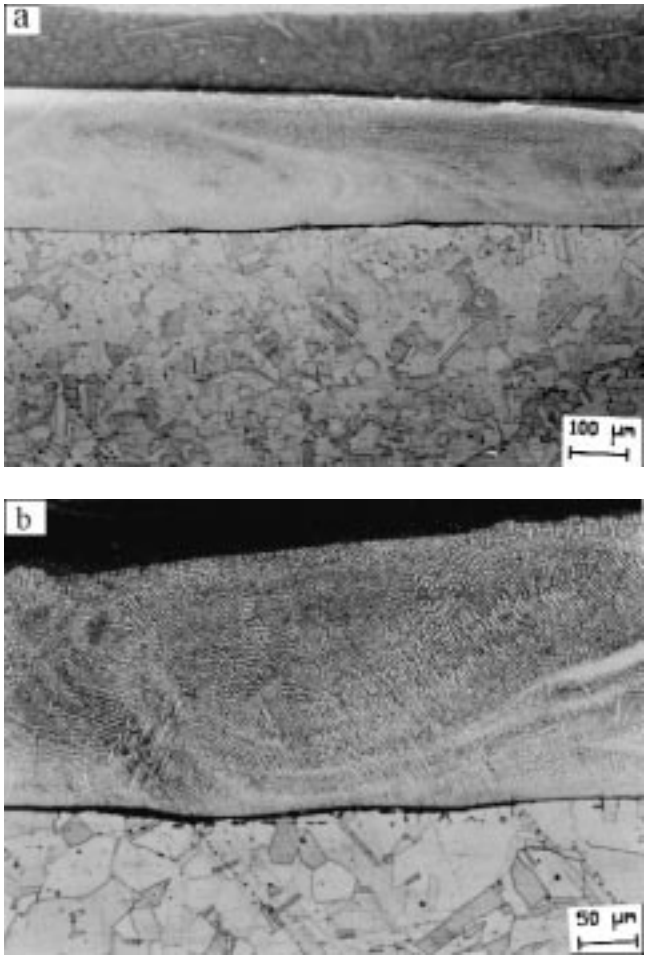

Fig. 2 The smooth defect-free alloyed region of LSA- 4 (**a**) where very fine cells are found at the center and (**b**) the cellular-dendritic growth is found at the interface

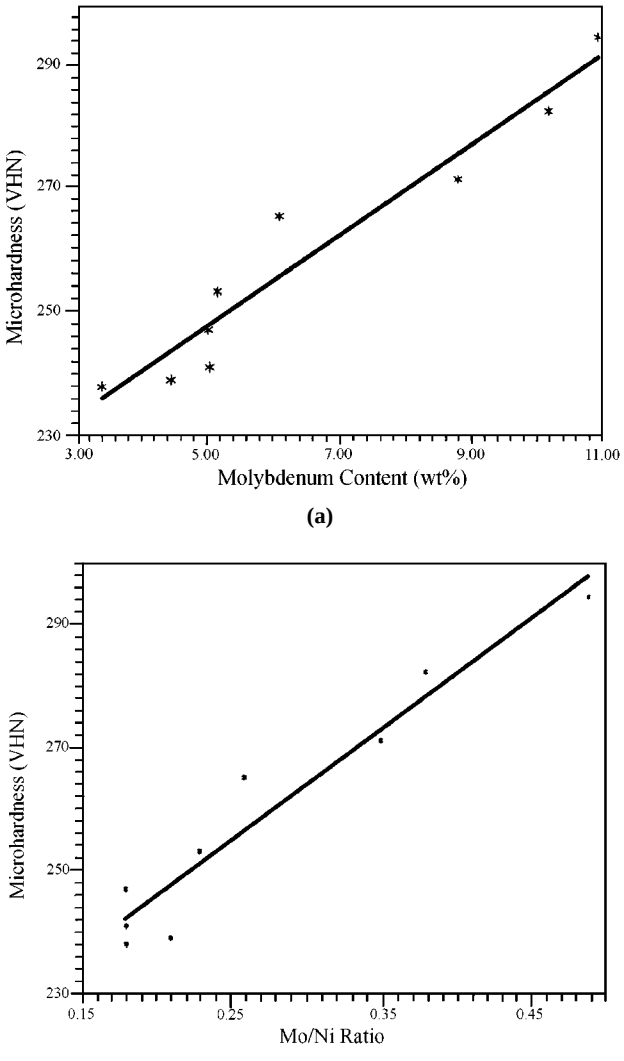

Fig. 3 Variation of microhardness (VHN) with (**a**) molybdenum content and (**b**) Mo/Ni ratio in the alloyed zone

tribute to the high hardness values observed, since the dislocation density in laser-treated stainless steels is very high.[9]

In LSA, a small melt pool is created at the surface. The temperature at the interface of the molten pool with the substrate (at the bottom and ends) will be that of the melting point of the substrate and the temperature will be high at the surface. This leads to varying surface tension values at different locations and surface tension driven fluid flow is generated, which leads to convection currents in the molten pool. These currents, responsible for mixing, are shown in Fig. 4 for samples LSA-1 to LSA-4. It can be seen that in LSA-1 and LSA-2, there is little porosity and the insufficient convection is clearly seen in LSA-1. Sample LSA-3 also exhibits very fine pores, whereas sample LSA-4 showed uniform convective mixing indicative of chemical homogeneity. The microstructure of these samples was also observed at higher magnifications and revealed cracks and porosity in LSA-1 and LSA-2, whereas LSA-3 and LSA-4 exhibited a crack-free microstructure (Fig 5). Since the Cr_{eq}/Ni_{eq} of these alloys favors primary austenite solidification, then the heat input has to be minimum to avoid cracking. Thus, in the case of LSA-3 and LSA-4, there was no cracking, since, in these cases, the heat input is low and, correspondingly, the cooling rate is higher. All laser-alloyed samples, when etched with modified Murakami's agent, indicated the absence of any secondary phases in spite of higher molybdenum contents. This is due to high cooling and solidification rates inherent to laser surface processing, which eliminates secondary phase formation.

The microstructures at the top and bottom of the laser-alloyed zones for LSA-1 to LSA-4 were studied by scanning electron microscopy (SEM), and the primary dendrite arm spacing (DAS) measurements were carried out both at the top and bottom of laser-alloyed samples (LSA-1 to LSA-9) using an image analyzer. For each sample, DAS measurements of six fields were taken, for the top and bottom portions, and their average value is reported in Table 4.

Since the DAS is an indication of the cooling rates involved in a rapid solidification process, the measured DAS near the surface was correlated with the calculated cooling rates. For calculating the cooling rates, the following relation, established by Brenian and Kear in Ref 10, was used. In this model, the tem-

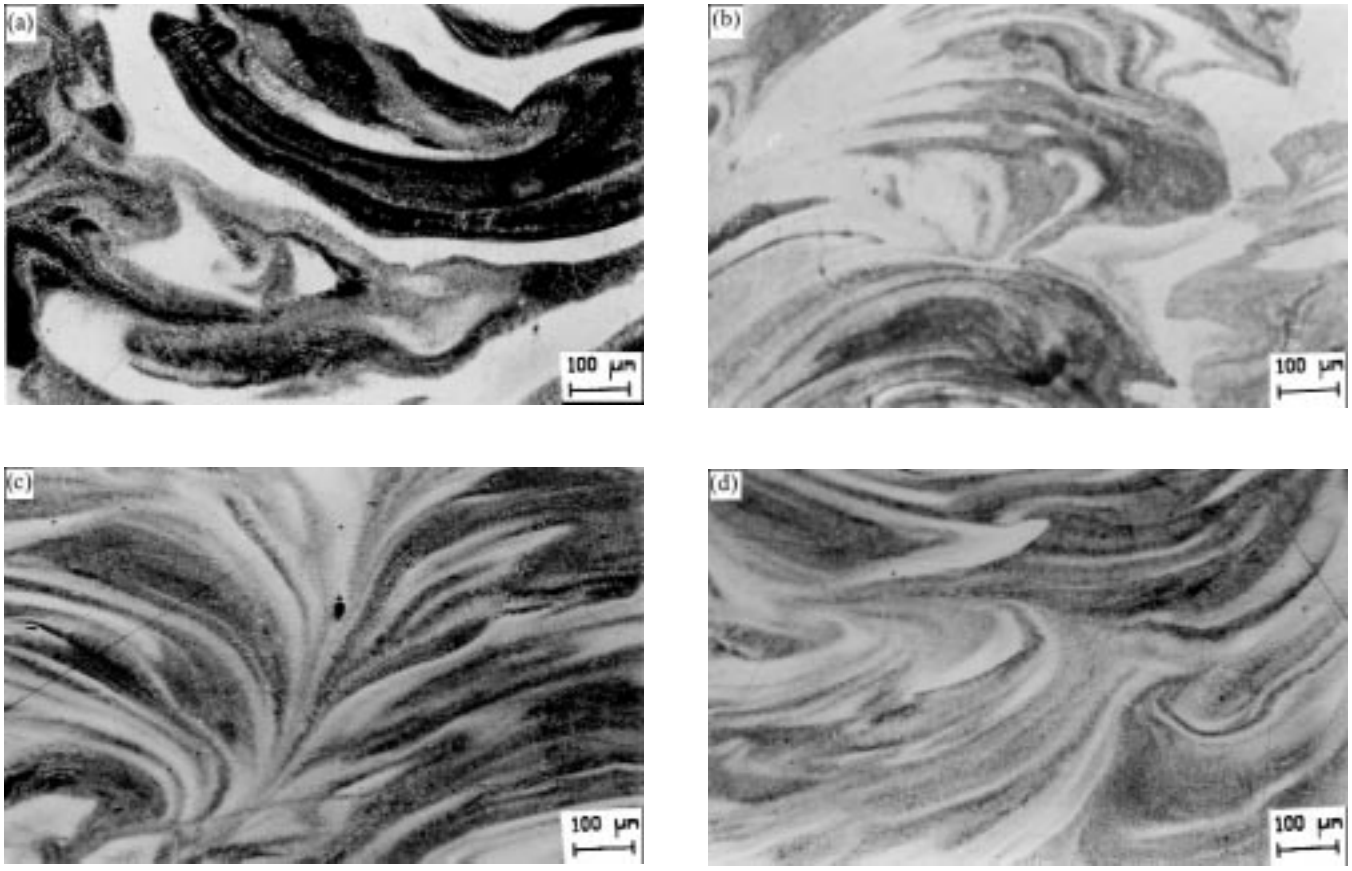

Fig. 4 The surface morphology of etched laser-alloyed samples of (**a**) LSA-1, (**b**) LSA-2, (**c**) LSA-3, and (**d**) LSA-4

Table 3 Microhardness of laser-alloyed zones

Sample	Avg. (VHN)
LSA-1	271
LSA-2	265
LSA-3	282
LSA-4	294
LSA-5	247
LSA-6	241
LSA-7	238
LSA-8	253
LSA-9	239

Table 4 DAS at the surface and bottom region of the laser-alloyed zone

Sample number	DAS μm surface	DAS μm bottom
LSA-1	4.36	5.42
LSA-2	3.54	4.63
LSA-3	2.81	3.46
LSA-4	2.15	2.98
LSA-5	1.92	2.03
LSA-6	2.26	3.27
LSA-7	3.21	4.06
LSA-8	3.94	4.46
LSA-9	3.73	4.14

perature-dependent thermal conductivity and thermal diffusivity are not considered.

$$\delta T/\delta t = q_0/k\ \{(\alpha/\pi t)^{1/2}{}_e - \{x/(4\alpha t)^{1/2}\}^2 — (\alpha/\pi\gamma)^{1/2}{}_e - \{x/4\ \alpha\gamma)^{1/2}\}^2\ \} \quad \text{(Eq 1)}$$

where q_0 = absorbed power density (W/cm^2),
k = thermal conductivity (W cm^{-1} C),
a = thermal diffusivity (cm^2/s)
t = time (s)
x = depth (cm)
$g = t - \tau$ (s)
t = interaction time (s).

An absorbed power density of 0.41% was chosen and the cooling rate (C) was calculated from the thermophysical properties of AISI type 304 stainless steel. Table 5 presents the values of solidification rate (R) and temperature gradient (G) at the surface. The solidification rate was determined by using the value of solidification time, calculated from Eq 1, and the experimentally determined melt depth, and the temperature gradient was determined from the relation $C = G{\cdot}R$. From Table 5, it is evident that even though the cooling rate is high for LSA-5, it possesses the lowest solidification time, the lowest power density, and, therefore, a lower temperature gradient, which leads to

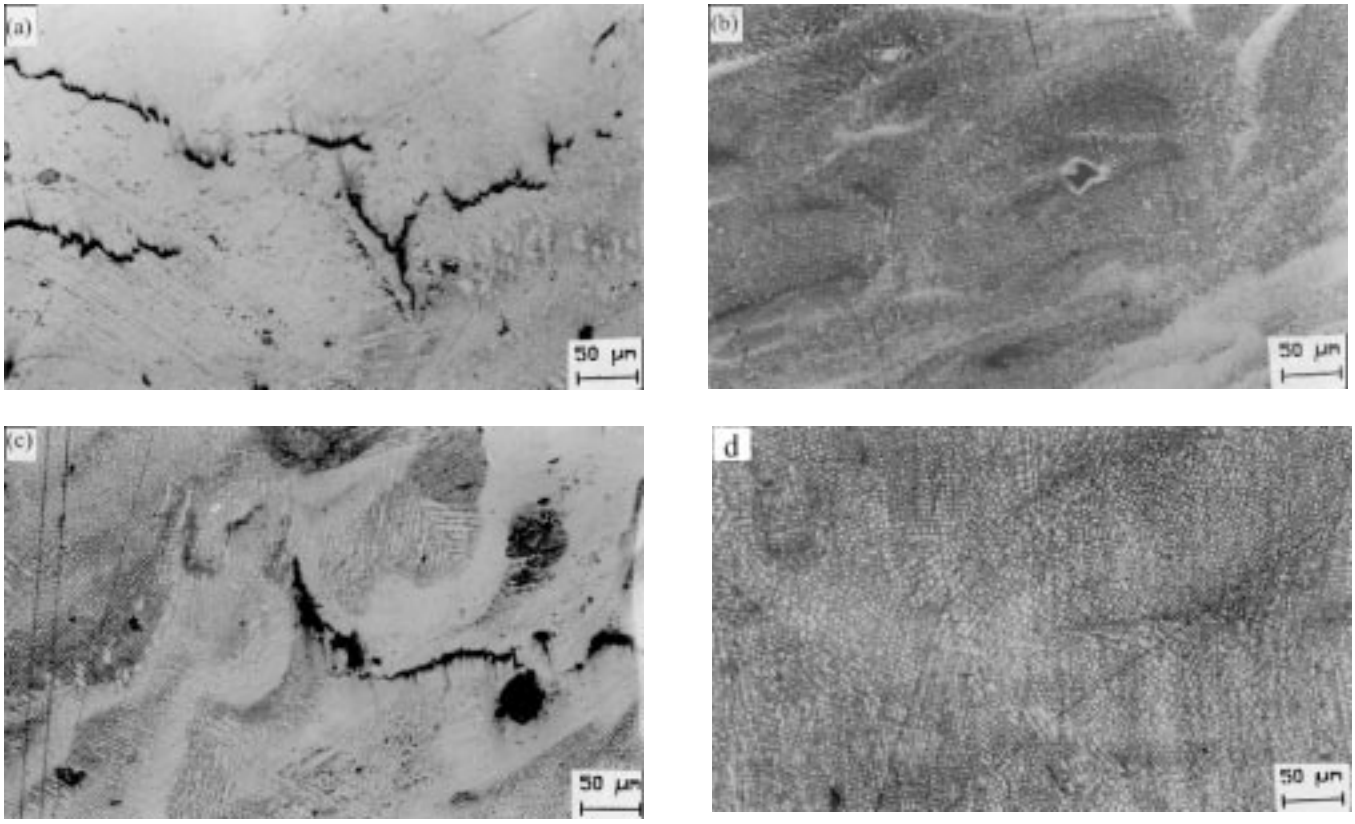

Fig. 5 The surface microstructure of (**a**) LSA-1, (**b**) LSA-2, (**c**) LSA-3, and (**d**) LSA-4

Table 5 Interaction time, solidification time, solidification rate, cooling rate, temperature gradient, and DAS of laser-alloyed samples

Sample	Interaction time τ(ms)	Solidification time τ*(ms)	Solidification rate $R \times 10^{-3}$ (m/s)	Cooling rate °C/s	Temp. gradient $\times 10^6$ (°C/m)	DAS (μm) at surface
Table 8A Varying scan speed						
LSA-1	60.0	407.0	0.9951	1603	1.6109	4.3693
LSA-2	39.6	180.4	2.1231	3512	1.6542	3.5498
LSA-3	30.0	100.0	3.6100	6131	1.6983	2.8184
LSA-4	24.0	58.0	7.4483	10,085	1.3540	2.1572
Table 8B Varying power						
LSA-5	39.6	6.04	60.2649	40,581	0.6734	1.9273
LSA-6	39.6	68.30	6.3104	8149	1.2914	2.2656
LSA-2	39.6	180.40	2.1231	3512	1.6542	3.5498
LSA-7	39.6	333.40	1.2747	1982	1.6983	3.2198
Table8C Varying spot size.						
LSA-2	39.6	180.40	2.1231	3512	1.6542	3.5498
LSA-9	60.0	175.00	3.7087	3453	0.9311	3.7321
LSA-8	79.8	165.20	4.1344	3485	0.8429	3.9426

insufficient convection mixing and chemical heterogeneity. Also, the next higher value of 1×10^5 was found in LSA-4. In this case, due to a higher power density and higher scan speed, the convective mixing is very good and the material has shown good homogeneity. Further, the temperature gradient is higher in the case of LSA-4 than LSA-5. It was shown in Ref 11 that, with increasing scan speed, the velocity of recirculating flow due to convection also increases by an order of magnitude. The measured DAS (d) at the surface was correlated with the calculated cooling rate, and the best fit is represented by

$$d = 39.81\ (\delta T/\ \delta t)^{-0.317} \qquad \text{(Eq 2)}$$

The plot of DAS with the cooling rate is shown in Fig. 6. The exponent value of –0.317 is in agreement with the reported value of –0.320 for stainless steels.[23] In Fig. 7(a), the cooling rate is plotted with respect to scan speed for samples LSA-1 to LSA-4. The graph indicates that with increasing scan speed, the cooling

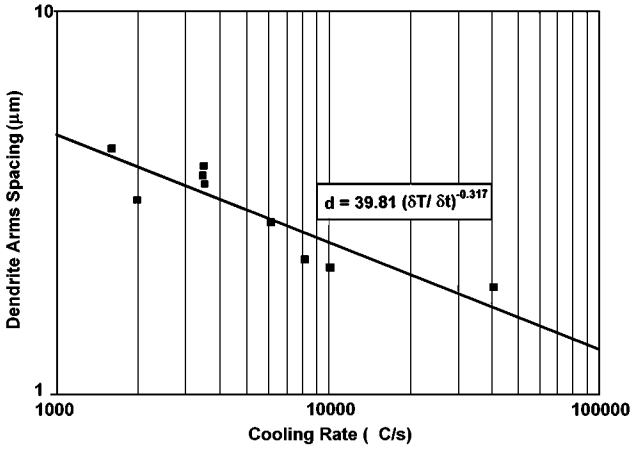

Fig. 6 Correlation between observed DAS and the calculated maximum cooling rate

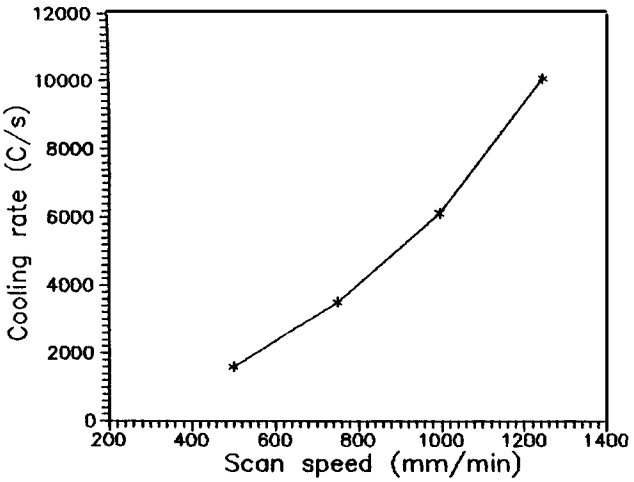

(a)

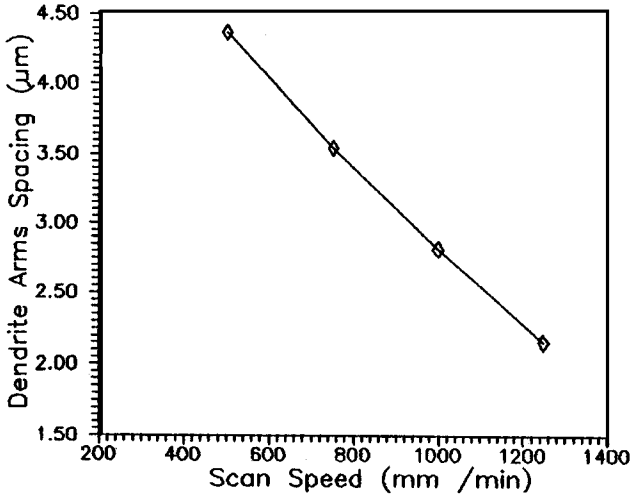

(b)

Fig. 7 Variation of (**a**) cooling rate and (**b**) DAS with scan speed

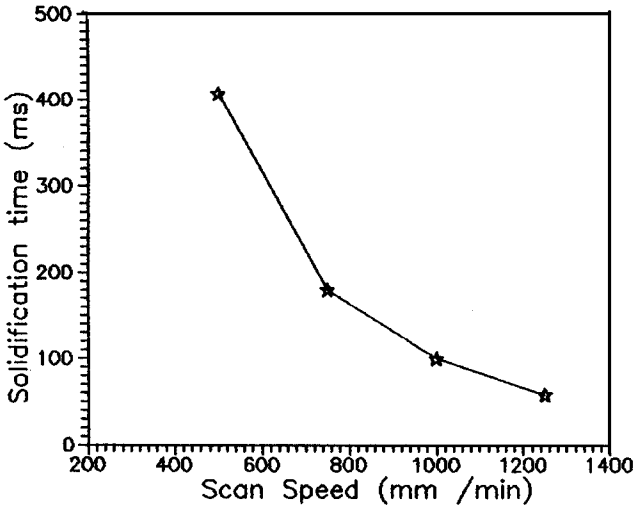

(a)

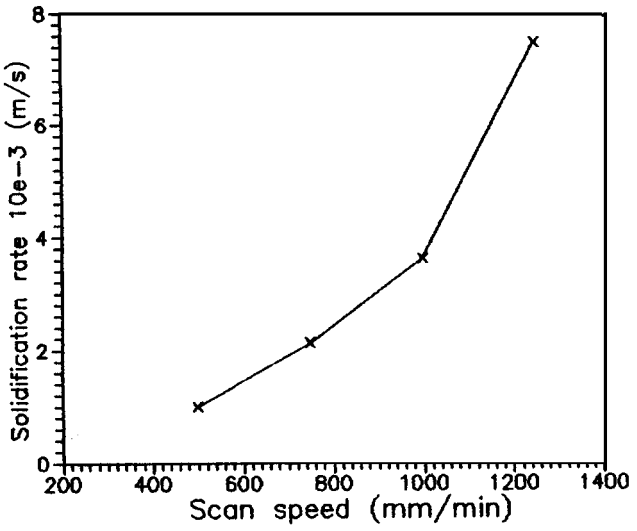

(b)

Fig. 8 Variation of (**a**) solidification time and (**b**) solidification rate with scan speed

rate increases due to reduced interaction time. This results in finer dendrite spacings with increasing scan speed, *i.e.*, with increasing cooling rate (Fig. 7b). In Fig. 8(a), the variation of solidification time with respect to scan speed is plotted. From this, it is evident that with increasing scan speed, the solidification time is decreased. Decreased solidification time indicates increased solidification rate for the molten pool. Thus, the solidification rate also increases with scan speed (Fig. 8b) and leads to finer microstructures. Here, even though the temperature gradient at the surface of sample LSA-4 is slightly lower (Table 5), this value has been found, when coupled with higher cooling and solidification rates, to form a highly homogeneous and fine microstructure.

The major effects of varying thermal conditions on solidification microstructure are well established. Increasing the gradient rate ratio (*i.e.*, the ratio of *G/R*) causes a progressive change

in the solidification characteristics, ranging from fully dendritic to cellular dendritic and then to planar front growth. On the other hand, increasing the cooling rate, or gradient rate product ($C = G \cdot R$), gives rise to shorter diffusion paths and finer structures. In other words, the ratio G/R controls the character of the microstructure, whereas the product $G \cdot R$ determines the scale of the microstructure. The solidification begins at the interface between the melted laser-alloyed zone and the base metal. Initially, a plane front growth corresponding to a light band at the bottom of the microstructure is observed, adjacent to the partially melted zone in the base metal (Fig 9). This phenomenon arises due to the fact that the growth velocity R starts from zero at the interface to its maximum value at the top of the laser-alloyed zone. At the same time, the temperature gradient G also decreases, thereby leading to a considerable decrease in G/R ratio up to the critical value G/R_{crit} defined in the constitutional supercooling theory.[12, 13] At this value, the planar front growth, starting from the interface, becomes unstable and, subsequently, a fine structure is formed. In the vicinity of the center of the laser-alloyed region, with a further increase in solidification rate, a typical dendritic-to-cell transition is observed and a superfine cellular structure is formed (Fig. 1d). At the top of the melted zone, fine dendrites appear and this could be ascribed to the fact that the molten pool is often sufficiently undercooled in laser processing and considerable nuclei are always found in the melt for rapid solidification.[14]

After laser processing, the surfaces of the alloyed layer were covered with a thin layer of oxide. As the shielding gas (He) was blown at the laser-spot location, the shielding gas was effective only during the interaction time of the laser beam with the target. However, the pool would remain molten, for a small finite time, even after the laser beam was moved to the next location. In this time interval, the alloying elements in the molten pool would interact with ambient air leading to the formation of various oxides. The oxides thus formed on the surface of the sample were characterized by XRD. The oxides formed on the surface of various alloys indicated the presence of spinel oxides in addition to chromium oxide and magnetite. The various oxides formed could not be correlated with the laser processing parameters, *i.e.*, with the surface temperature, because the oxides formed at the center and at the ends of the pool were different due to varying cooling rates at these locations. The XRD pattern of the laser-alloyed samples, taken after removing 50 μm from the surface (to remove surface oxide), indicated the presence of the desired austenitic phase as that of the base metal.[15]

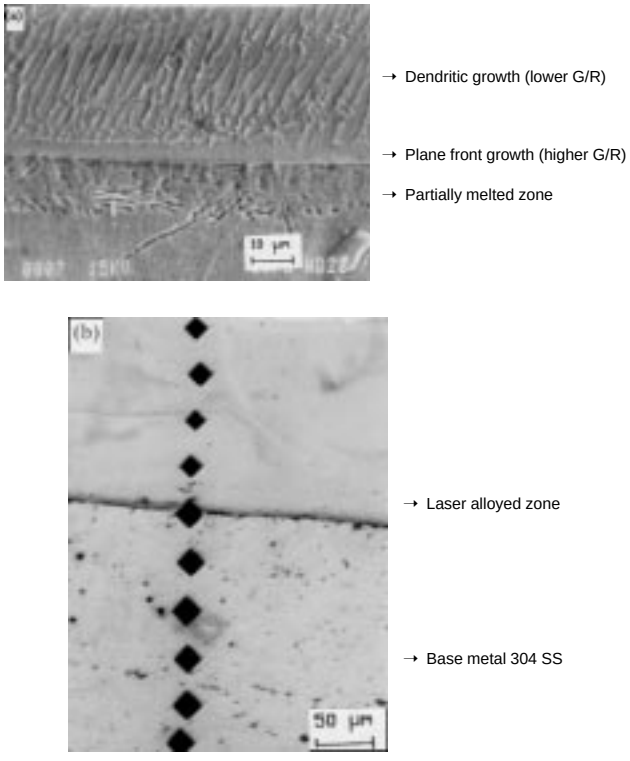

Fig. 9 (**a**) Effect of G/R ratio on the microstructure of the laser-alloyed zone and (**b**) micrograph showing indentation marks during microhardness determination

3.2 Chemical Composition and Solidification Mode

Table 6 gives the chemical composition, which is an average of three fields taken at the center of the alloyed zone from top to bottom. Reasonably good homogeneity was found in all the samples, with minor fluctuations in the range of ±2 wt.% of molybdenum content. With increasing power, the fluctuations were found to decrease. This effect may be due to increased power density and associated vigorous fluid flow in the molten pool, leading to better homogeneity. The fluctuation also decreased with increasing spot size, most probably due to increased interaction time of the laser beam with the molten pool. The composition profiles of laser-alloyed samples of varying scan speeds at constant power, viz., LSA-1 to LSA-4, were determined at every 50 micrometers and the Mo contents. Molybdenum in these alloys is presented in Table 7. Also given in the table is the percentage variation of molybdenum with the average value. The graphical representation of these is shown in Fig 10. From this, it is evident that the variation in Mo content with that of the average value was as high as 7 to 25 wt.% for LSA-1, LSA-2, and LSA-3, whereas for LSA-4, it was only 0.3 to 6 wt.%. This clearly indicates the better homogeneity of LSA-4 compared to other alloys, which may have higher molybdenum contents.

Conventionally used highly alloyed austenitic stainless steels usually have their composition adjusted such that there is about 5 to 8% delta ferrite in the microstructure. Small amounts of delta ferrite can take into solid solution elements such as sulfur, phosphorus, silicon, and manganese, thus leading to increased

Table 6 Compositional analysis of laser-alloyed samples

Sample	Wt.% Cr	Ni	Mo	Fe
LSA-1	17.85	24.84	8.79	48.52
LSA-2	18.65	23.66	6.10	51.59
LSA-3	16.57	26.54	10.19	46.70
LSA-4	17.41	22.46	10.95	49.18
LSA-5	17.60	27.39	5.03	49.98
LSA-6	17.52	27.47	5.05	49.96
LSA-7	18.54	18.62	3.40	59.44
LSA-8	18.24	22.56	5.17	54.03
LSA-9	18.11	21.34	4.46	56.09

Table 7 Composition analysis of Mo content in alloys LSA-1 to LSA-4 at successive depths of 50 μm from the surface

LSA-1								
Distance from surface (μm)	50	100	150	200	250	300	350	400
Mo wt.%	7.76	8.49	8.10	6.20	5.12	6.52	7.92	6.13
Variation in Mo (%)	10.40	20.77	15.22	11.81	27.17	7.25	12.66	12.80
Average Mo (wt.%) = 7.03								
LSA-2								
Distance from surface (μm)	50	100	150	200	250	300	350	
Mo wt.%	6.63	6.03	5.59	5.21	4.95	4.51	5.53	
Variation in Mo (%)	20.80	9.84	1.64	5.10	9.84	17.85	0.73	
Average Mo (wt.%) = 5.49								
LSA-3								
Distance from surface (μm)	50	100	150	200	250	300	350	
Mo wt.%	11.17	10.08	9.82	9.07	8.01	8.13	8.95	
Variation in Mo (%)	19.85	8.15	5.36	2.68	14.06	12.77	3.97	
Average Mo (wt.%) = 9.32								
LSA-4								
Distance from surface (μm)	50	100	150	200	250	300	350	400
Mo wt.%	12.16	11.50	11.20	10.90	11.53	12.10	10.92	11.42
Variation in Mo (%)	6.02	0.26	2.35	4.96	0.52	5.49	4.80	0.44
Average Mo (wt.%) = 11.47								

crack resistance of the alloy.[16] Also, in the conventionally alloyed steels, the alloys that solidify primarily as ferrite have better cracking resistance than those that solidify as austenite.[17] Though ferrite has been found to reduce the hot cracking resistance of austenitic stainless steel weldments, it may lead to decreased corrosion resistance and embrittlement at high temperatures. Hence, it is desirable to produce a fully austenitic microstructure without any propensity to hot cracking.[18] All the conventional methods of processing result in higher heat input, thereby increasing the tendency toward hot cracking.

Rapid solidification provides one way of altering the normal solidification structure. The formation of high temperature and/or equilibrium structures can be suppressed due to large undercooling and high cooling rates encountered during rapid solidification, leading to a variety of new structures, including metastable nonequilibrium phases. Laser surface processing is one such rapid solidification technique. In this technique, due to decreased heat input associated with high cooling rates inherent in the process, it is possible to produce crack-free fully austenitic microstructures without any traces of delta ferrite.[17] In the surface alloys processed (LSA-1 to LSA-9), nickel was increased to favor the austenitic phase. Increasing molybdenum content alone (for increased pitting resistance) will lead to the formation of delta ferrite. In all the alloys, a fully austenitic microstucture was found in spite of very high molybdenum (10 to 13 wt.%). This was made possible due to high cooling rates and associated undercooling of the samples. Because of their homogeneous structure, fully austenitic steels possess excellent corrosion resistance and toughness properties.

The chromium and nickel equivalents (Cr_{eq} and Ni_{eq}) with respect to the compositions of the laser-alloyed zone were determined using the following empirical relation:[18]

$$Cr_{eq} = 1Cr + 1Mo + 1.5Si + 0.5Nb$$

$$Ni_{eq} = 1Ni + 30C + 0.5Mn$$

where the symbols denote the elemental compositions in weight percent. The ratio of Cr_{eq}/Ni_{eq} for each surface alloy is given in Table 6.

The Schaffler diagram is a plot of chromium and nickel equivalents of stainless steels with lines delineating austenitic, ferritic, and austenitic + ferritic structures and is useful for predicting phases in stainless steels formed by conventional melting procedures (*i.e.*, equilibrium is maintained). Recently, David *et al.*[21] reported on a modified Schaffler diagram, which incorporates high cooling rates involved in welding process. This diagram indicated a relation between Cr and Ni equivalents and the phases present in the microstructure. At low cooling rates, the contour lines are similar to the original Schaffler diagram, since the dependence of microstructure on cooling rate is low; whereas at high cooling rates, the lines representing 0 and 10 wt.% ferrite tend to converge, indicating reduced delta ferrite in the microstructure with increasing cooling rates.

It has been reported that when the ratio of Cr_{eq}/Ni_{eq} is lower than 1.35, solidification results in austenite formation, and when it is greater than 1.35, ferrite is formed.[22] The ratio of Cr_{eq}/Ni_{eq} for each surface alloy is given in Table 7, and from this, it is expected that all experimental surface alloys should get solidified in primary austenitic solidification mode. By plotting the Cr_{eq} and Ni_{eq} of the surface alloys on these modified diagrams for various cooling rates, it was predicted that these alloys would have

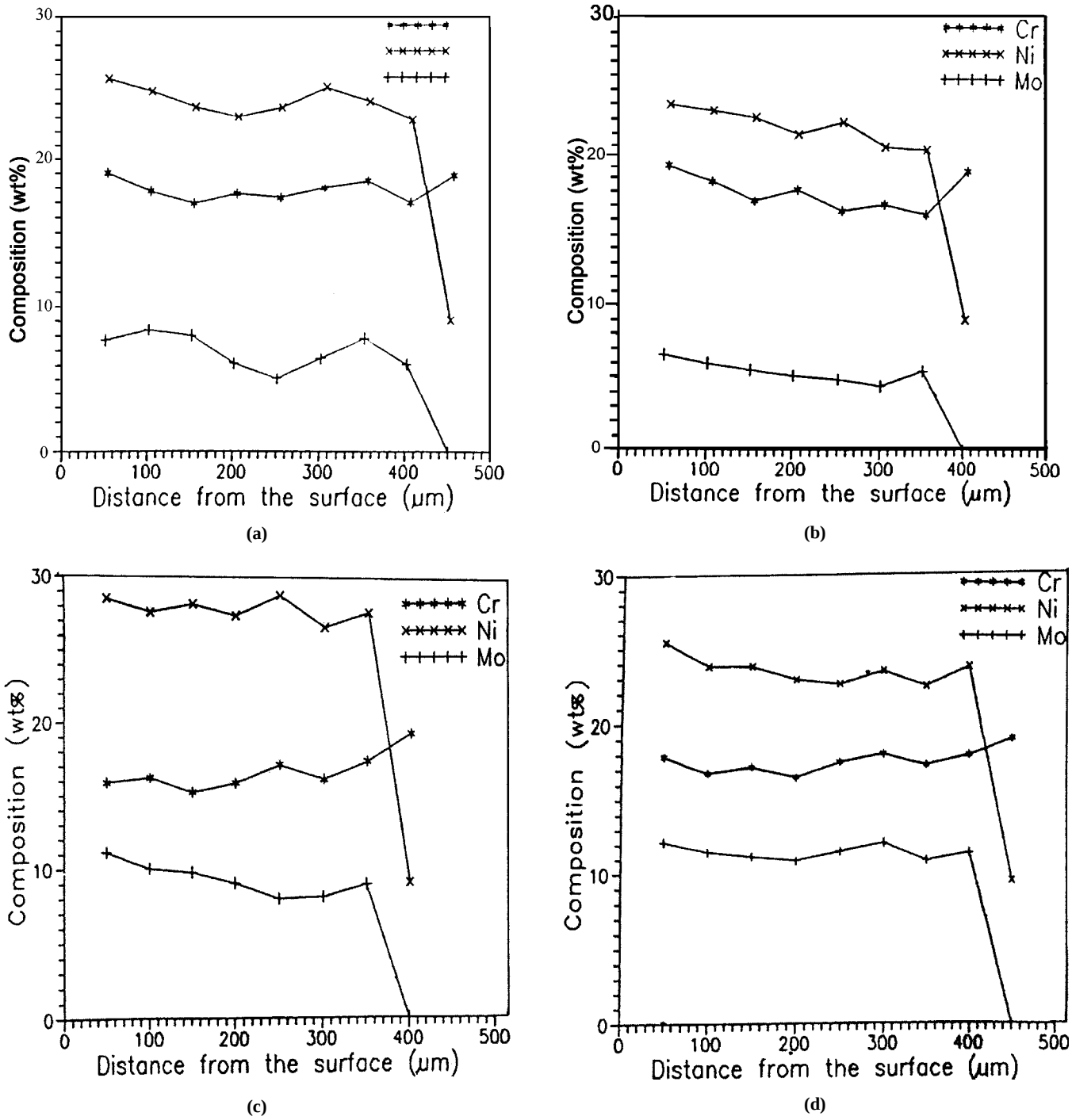

Fig. 10 Composition profile of alloying elements in (**a**) LSA-1, (**b**) LSA-2, (**c**) LSA-3, and (**d**) LSA-4 as a function of depth from the surface

austenite phase at all cooling rates. The microstructure found confirmed this prediction.[15]

In the present study, due to a lower Cr_{eq}/Ni_{eq} of 0.8 to 1.2 for samples of LSA-1 to LSA-9, all the alloys exhibited austenitic microstructure. However, the samples of LSA-1 (Fig. 5a) and LSA-2 (Fig. 5b) showed the presence of cracks and porosity. This arises since the heat input is relatively high and, hence, leads to formation of austenite and associated cracking. However, when the scan speed is increased to 1000 and 1250 mm/min (LSA-3 and LSA-4), the heat and, hence, the cooling rate input are reduced. This results in the formation of a crack-free, smooth, laser-alloyed zone. Also Katayama *et al.*[23] investigated the CW laser welding of austenitic stainless steels with Cr_{eq}/Ni_{eq} of 1.1506 at various speeds and found that the microstructure was fully austenitic with no residual ferrite or cracks.

Table 8 Chromium and nickel equivalent of alloyed samples

Sample	Cr_{eq}	Ni_{eq}	Cr_{eq}/Ni_{eq}
LSA-1	27.38	26.24	1.043
LSA-2	25.49	25.06	1.010
LSA-3	27.50	27.94	1.016
LSA-4	29.10	23.86	1.219
LSA-5	23.37	28.79	0.812
LSA-6	23.31	28.87	0.807
LSA-7	22.68	20.02	1.133
LSA-8	24.15	23.96	1.008
LSA-9	23.31	22.74	1.025

AISI type 304 SS generally solidifies in the primary ferrite solidification mode ($Cr_{eq}/Ni_{eq} = 1.91$) When the value of Cr_{eq}/Ni_{eq} for 304 SS is plotted on a modified Schaffler diagram for various cooling rates, the location of 304 SS is shifted above the 0 contour line, thereby indicating the absence of delta ferrite.[15] Thus, with the increasing cooling rate (increasing the scan speed, at constant power), the absence of ferrite was observed. The solidification sequence changes from

$$L \rightarrow L + \delta \rightarrow \delta \rightarrow \delta + \gamma \text{(for conventional welding processes)}$$

to

$$L \rightarrow L + \delta \rightarrow \delta \rightarrow \delta + \gamma \rightarrow \gamma \text{(for laser welding processes)} \quad \text{(Eq 3)}$$

In the laser surface alloys formed, due to their lower Cr_{eq}/Ni_{eq} values (0.8 to 1.2) (Table 8) and lower heat input, the formation of δ in Eq 3 does not occur and the following solidification sequence was observed:

$$L \rightarrow L + \gamma \rightarrow \gamma \quad \text{(Eq 4)}$$

The above sequences are supported by the study of Vitek *et al.*[19] and Suutala *et al.*[20] for rapidly solidifying 310 SS with Cr_{eq}/Ni_{eq} of 1.1.

During solidification of austenitic stainless steels, the austenite forming initially *i.e.*, at the core of the dendrites, is depleted in molybdenum or chromium and enriched in nickel. The interdendritic region, formed from the last liquid to solidify, therefore, would be enriched in chromium and depleted in nickel.[22] The enrichment of alloying elements at austenite cell boundaries has been observed by Takalo *et al.*[24] and Arata *et al.*[25] The degree of segregation has also been shown to be reduced by high cooling rates.[23] With increasing cooling rates, the microstructural features (including the scale of microstructure) become refined, because the time for coarsening during solidification is reduced. As a consequence, the DAS decreases with increasing cooling rate during solidification.

With increasing cooling rates (in our case, LSA-4), nucleation takes place at temperatures well below the liquidus (around 1400 °C), and there can be large departures from local equilibrium at advancing solid/liquid interfaces. Thus, the solid phase may entrap a supersaturated concentration of solute and impurity atoms such that the solid may have exactly the same composition as the parent liquid.

In the liquid state, diffusion is enhanced by convection movements in the melt pool. This phenomenon results from the existence of three forces: gravity, viscosity, and the surface tension gradient. Since temperature is not uniform in the melt zone and viscosity and surface tension are temperature dependent; mass transport is induced by these gradients. This is termed the "Marangoni effect" and enhances interdiffusion, which improves homogenization of the surface alloy.[26] This recirculating velocity of convective flow has been found to increase by an order of magnitude over the scanning speed of the laser.[14] Hence, in the present case, for sample LSA-4, the recirculating velocity of convective flow will be much higher than that of samples LSA-1 to LSA-3 due its increased scanning speed.

In the case of LSA, while solidification occurs *via* the formation of austenite, the dendrite core will be deficient in molybdenum and chromium since their partition coefficients (*i.e.*, the ratio of the concentration of alloying element in the liquid to that of solidifying crystals (solid) [$k_0\gamma$(Cr) = 0.80, $k_0\gamma$(Mo) = 0.65)]) are less than unity. Thus, in the case of surface alloys LSA-1 and LSA-2, the compositional profile of alloying elements indicates microsegregation leading to poor corrosion behavior.[27] The sample LSA-3 also indicated microsegregation to a lesser degree, whereas in the case of LSA-4 (scan speed: 1250 mm/min), the segregation is minimal. Sample LSA-4 underwent the lowest interaction and solidification time, which resulted in increased solidification and cooling rate. Also, due to increased available power for LSA-4 (since absorption of the laser beam by the plasma is minimal in this case), the actual temperature gradient will be higher across the surface, leading to efficient convective mixing in the molten pool. All these factors have led to finer microstructure with improved chemical homogeneity leading to improved corrosion behavior.[27] Also, improved chemical homogeneity of the alloy with increased laser scanning speed was observed by Nakao *et al.*[28] during their experiments on laser surface melting of high alloy SS such as 904 L (26% Ni, 21% Cr, and 5% Mo). Their experimental findings were also validated by the Kurz-Gianovola-Trivedi model, which was used to calculate the composition at the dendrite tip. Both Cr and Mo concentrations at the dendrite core were found to increase with increasing solidification rate (scan speed) and to approach the average concentration at higher solidification rates. This indicates that the solute profile across the cells becomes even with the increasing solidification rate and finally homogeneous above the critical solidification rate. Thus, in the case of LSA-4, the critical solidification rate is exceeded or just achieved, as evidenced by the compositional homogeneity of the surface.

The segregation is significantly reduced in fine dendrites and cells after laser solidification processing, and the microsegregation in the superfine cellular crystals is almost completely eliminated, as was found in LSA-4 (Fig. 1d). Two mechanisms may be correlated to the remarkable improvement of the segregation degree. One is the microstructural refinement, which enables the interdendritic or intercellular homogeneity, and the other is that the nonequilibrium partition coefficient tends to unity with an increase in the solidification rate.[29]

4. Conclusions

- Superaustenitic SS surface alloys were formed with high molybdenum contents (3 to 12 wt.%) using LSA on AISI type 304 SS. There was no evidence of secondary phases

(intermetallic compounds) such as sigma and chi in spite of higher molybdenum contents.

- The effect of laser processing parameters on the composition and microstructural characteristics of the laser-alloyed zone was studied. This led to identification of optimized laser processing parameters, viz., power of 3 kW, scan speed of 1250 mm/min, and a laser spot size of 0.5×1.00 mm for forming surface alloys with good compositional and microstructural homogeneity.
- Correlation between the theoretically calculated cooling rate and measured DAS in the laser-surface-alloyed zones was found to be in good agreement.
- Changes in solidification mode due to laser surface processing was correlated with cooling rates and processing conditions.
- Iincreased velocity of recirculating convection currents in the molten pool in composition LSA-4 (power = 3 kW, scan speed = 1250 mm/min, and spot size = 0.5×6 mm) contributes to very good compositional homogeneity.

Acknowledgments

The authors are grateful to Dr. K. Wissenbach, Fraunhofer Institut for Lasertechnik Aachen, for providing the laser facilities to carry out this job. Mr. Dhimant Doshi, Plasma Spray Processes, and Mr. Purandare, TIFR, are thankfully acknowledged for their help in plasma coating and EDAX of alloyed samples, respectively.

References

1. A.J. Sedriks: in *Corrosion of Stainless Steels*, John Wiley, New York, NY, p 63.
2. J.R. Kearns: *J. Mater. Energy Systems*, 1985, vol. 7, p 16.
3. E. Wallis: *Werkst. Korr.*, 1990, vol. 41, p 41.
4. T.P.S. Gill, J.B Gnanamoorthy, and K.A. Padmanabhan: *Corrosion*, 1984, vol. 43, p 208.
5. K. Komvopouloulos and K. Nagarathnam: *Trans. ASME, J. Eng. Mater. Technol.*, 1990, p 131.
6. C.W. Draper and J.M. Poate: *Int. Met. Rev.*, 1985, vol. 30, p 85.
7. D. Kumar, K. Sridhar, A.R. Biswas, G.L. Goswami, and M.B. Deshmukh: *J. Laser Appl.*, 1993, vol. 5, p 23.
8. T. Wada: *Metals Handbook*, 8th ed., ASM, Cleveland, OH, 1973, p 409.
9. P.A. Molian and W.E. Wood: *J. Mater. Sci.*, 1983, vol. 18, p 2563.
10. E.M. Breinan and B.H. Kear: in *Laser Materials Processing*, M. Bass, ed., North Holland Publishing Company, 1983, p 239.
11. T. Chande and J. Mazumdar: *J. Appl. Phys.*, 1995, vol. 57, p 2226.
12. W.A. Tiller, K.A. Jackson, J.W. Ritter, and B. Chalmers: *Acta Metall.*, 1953, vol. 1, p 458.
13. L. Renaud, B. Cabaud, F. Fouquet, H. Mazille, and J.L. Crolet: *Key Eng. Mater.*, 1990, vols. 46-47, p 305.
14. S. Kou and Y. Le: *Metall. Trans. A*, 1988, vol. 19A, p 1075.
15. K. Sridhar, A.S. Khanna, A. Gasser, and M.B. Deshmukh: *Lasers Eng.*, 1996, vol. 5, p 107.
16. J.C. Borland and R.N. Younger: *Br. Welding J.*, 1960, vol. 7, p 22.
17. F.C. Hull: *Welding J.*, 1967, vol. 46, p 399.
18. Y. Arata, T. Matsuda, and S. Katayama: *Trans. JWRI*, 1976, vol. 5, p 35.
19. J.M. Vitek, A. Dasgupta, and S.A. David: *Metall.Trans. A*, 1983, vol. 14A, p 1833.
20. N. Suutala, T. Takalo, and T. Moisio: *Metall. Trans. A*, 1979, vol. 10A, p 512.
21. S.A. David, J.M.Vitek, and T.L. Hebble: *Welding J.*, 1987, vol. 66, p 289.
22. J.C. Lippold and W.E. Savage: *Welding J.*, 1979, vol. 58, p 362.
23. S. Katayama and A. Matsunawa: *Proc. Int. Conf. on Lasers and Electro-optics'85*, San Francisco, CA, 11-14 November 1985, paper no.506.
24. T. Takalo, N. Suutala, and T. Moisio: *Metall. Trans. A*, 1979, vol. 10A, p 1173.
25. Y. Arata, T. Matsuda, and S. Katayama: *Trans. JWRI*, 1976, vol. 5, p 35.
26. J.M. Pelletier, S. Jobez, Q. Saif, P. Kirat, and A.B. Vannes*: J. Mater. Eng.*, 1991, vol. 13, p 281.
27. K. Sridhar, A.S. Khanna, K. Wissenbach, and M.B. Deshmukh: *Proc. Corrosion/98*, San Diego, CA, Mar. 22-27, 1998, paper no. 705 (on CD-ROM).
28. Y. Nakao and K. Nishimoto: *Iron Steel Inst. Jpn. Int.*, 1993, vol. 33, p 934.
29. O.Y. Pan *et al.:* J. Mater. Sci. Lett., 1996, vol, 15, p 2112.